

Atmospheric scattering of energetic electrons from near-Earth space

Vassilis Angelopoulos (✉ vassilis@ucla.edu)

University of California Los Angeles <https://orcid.org/0000-0001-7024-1561>

Ethan Tsai

University of California Los Angeles

Colin Wilkins

University of California Los Angeles

Xiaojia Zhang

University of California Los Angeles

Anton Artemyev

University of California

Jiang Liu

University of California Los Angeles

Andrei Runov

University of California Los Angeles

Laura Iglesias

University of California Los Angeles

Drew Turner

The Aerospace Corp.

Robert Strangeway

Institute of Geophysics and Planetary Physics, UCLA

Richard Wirz

University of California Los Angeles

Wen Li

Boston University

Lydia Adair

University of California Los Angeles

Ryan Caron

University of California Los Angeles

Maxwell Chung

Johns Hopkins University, Applied Physics Laboratory

Patrick Cruce

Apple

Eric Grimes

University of California Los Angeles

Kathryn Hector

Raytheon Space and Airborne Systems

Michael Lawson

University of California Los Angeles

David Leneman

University of California Los Angeles

Emmanuel Masongsong

University of California Los Angeles <https://orcid.org/0000-0002-0266-6864>

Austin Norris

University of California Los Angeles

Cynthia Russell

University of California Los Angeles

Christopher Shaffer

Tyvak Nano-Satellite Systems

Jiashu Wu

University of California Los Angeles

Sharvani Jha

University of California Los Angeles

James King

University of California Los Angeles

Suyash Kumar

University of California Los Angeles

Kelly Nguyen

University of California Los Angeles

Michelle Nguyen

University of California Los Angeles

Akhil Palla

University of California Los Angeles

Alexa Roosnov

University of California Los Angeles

Erica Xie

University of California Los Angeles

Rebecca Yap

University of California Los Angeles

Chanel Young

University of California Los Angeles

J. B. Blake

The Aerospace Corporation

Nick Adair

Millenium Space Systems

Matthew Allen

Northrop-Grumman Aerospace Systems

Michael Anderson

Lucid Motors

Michael Arreola-Zamora

Northrop-Grumman Aerospace Systems

Jessica Artinger

University of California Los Angeles

Jeffrey Asher

Johns Hopkins University, Applied Physics Laboratory

Donna Branchevsky

The Aerospace Corporation

Michael Capitelli

Millenium Space Systems

Rommel Castro

Raytheon Space and Airborne Systems

Gary Chao

Boeing

Nathan Chung

Tesla

Micah Cliffe

SpaceX

Kyle Colton

Planet Labs

Cian Costello

NovaSignal

Danny Depe

University of California Los Angeles

Benjamin Domae

University of California Los Angeles

Sarah Eldin

University of California Los Angeles

Lauren Fitgibbon

Tyvak Nano-Satellite Systems

Alex Flemming

Northrop-Grumman Aerospace Systems

Ian Fox

University of California Los Angeles

Duncan Frederick

Millenium Space Systems

Alex Gilbert

University of California Los Angeles

Anthony Gildemeister

Northrop-Grumman Aerospace Systems

Alexander Gonzalez

University of California Los Angeles

Brayden Hesford

Jet Propulsion Laboratory

Renee Krieger

Mercedes-Benz Research and Development North America

Kevin Lian

Northrop-Grumman Aerospace Systems

Jason Mao

Epic Systems Corporation

Emmons McKinney

California State Polytechnic University, Pomona

Jordan Miller

University of California Los Angeles

Matt Nuesca

University of California Los Angeles

Elisa Park

University of California Los Angeles

Carter Pedersen

University of California Los Angeles

Ziyuan Qu

University of California Los Angeles

Reuben Rozario

SpaceX

Erik Rye

University of California Los Angeles

Ryan Seaton

University of California Los Angeles

Akshaya Subramanian

Northrop-Grumman Aerospace Systems

Stephen Sundin

Tyvak Nano-Satellite Systems

Aysen Tan

Experior Laboratories

Wynne Turner

University of California Los Angeles

Austin Villegas

University of California Los Angeles

Matt Wasden

University of California Los Angeles

Graham Wing

University of California Los Angeles

Cass Wong

University of California Los Angeles

Anais Zarifian

Jet Propulsion Laboratory

Gary Zhang

University of California Los Angeles

Physical Sciences - Article

Keywords: Repopulation of the Magnetosphere, Radiation Belt Flux Evolution, Ozone Depletion, Global Atmospheric Circulation, Relativistic Electrons

Posted Date: March 12th, 2021

DOI: <https://doi.org/10.21203/rs.3.rs-319558/v1>

License:   This work is licensed under a Creative Commons Attribution 4.0 International License.

[Read Full License](#)

Atmospheric scattering of energetic electrons from near-Earth space

V. Angelopoulos^{1*}, E. Tsai¹, C. Wilkins¹, X.-J. Zhang¹, A. V. Artemyev¹, J. Liu¹, A. Runov¹, L. Iglesias¹, D. L. Turner², R. J. Strangeway¹, R. E. Wirz³, W. Li⁴, L. Adair^{1,5}, R. P. Caron¹, M. Chung², P. Cruce⁶, E. Grimes¹, K. Hector⁷, M. J. Lawson¹, D. Leneman¹, E. V. Masongsong¹, A. Norris¹, C. L. Russell¹, C. Shaffer⁸, J. Wu¹, S. Jha^{1,9}, J. King^{1,9}, S. Kumar^{1,10}, K. Nguyen^{1,3}, M. Nguyen^{1,11}, A. Palla^{1,9}, A. Roosnov^{1,10}, E. Xie^{1,11}, R. Yap^{1,12}, C. Young^{1,9}, J. B. Blake¹³, N. Adair⁵, M. Allen¹⁴, M. Anderson¹⁵, M. Arreola-Zamora^{1,14}, J. Artinger^{1,10}, J. Asher², D. Branchevsky¹³, M. R. Capitelli⁵, R. Castro^{7,9}, G. Chao^{3,16}, N. Chung¹⁷, M. Cliffe¹⁸, K. Colton¹⁹, C. Costello²⁰, D. Depe¹¹, B. W. Domae¹¹, S. Eldin¹¹, L. Fitzgibbon⁸, A. Flemming¹⁴, I. Fox³, D. M. Frederick⁵, A. Gilbert¹¹, A. Gildemeister¹⁴, A. Gonzalez⁹, B. Hesford²¹, R. Krieger²², K. Lian¹⁴, J. Mao²³, E. McKinney²⁴, J. P. Miller⁹, M. Nuesca⁹, E. S. Y. Park²⁵, C. E. Pedersen³, Z. Qu³, R. Rozario¹⁸, E. Rye¹¹, R. Seaton¹, A. Subramanian¹⁴, S. R. Sundin⁸, A. Tan²⁶, W. Turner¹⁰, A. J. Villegas¹⁰, M. Wasden³, G. Wing⁹, C. Wong¹⁰, A. Zarifian²¹, G. Y. Zhang²⁷

Affiliations:

- 1 Earth, Planetary, and Space Sciences Department, and Institute of Geophysics and Planetary Physics, University of California, Los Angeles, CA 90095
- 2 Johns Hopkins University Applied Physics Laboratory, Laurel, Maryland 20723
- 3 Mechanical and Aerospace Engineering Department, Henry Samueli School of Engineering, University of California, Los Angeles, CA 90095
- 4 Department of Astronomy and Center for Space Physics, Boston University, Boston, MA 02215
- 5 Millenium Space Systems, El Segundo, CA 90245
- 6 Apple Inc., Cupertino, CA 95014
- 7 Raytheon Space and Airborne Systems, El Segundo, CA 90245
- 8 Tyvak Nano-Satellite Systems, Inc., Irvine, CA 92618
- 9 Computer Science Department, Henry Samueli School of Engineering, University of California, Los Angeles, CA 90095
- 10 Physics and Astronomy Department, University of California, Los Angeles, CA 90095
- 11 Electrical and Computer Engineering Department, Henry Samueli School of Engineering, University of California, Los Angeles, CA 90095
- 12 Mathematics Department, University of California, Los Angeles, CA 90095
- 13 The Aerospace Corporation, El Segundo, CA 90245
- 14 Northrop Grumman Aerospace Systems, Redondo Beach, CA 90278
- 15 Lucid Motors, Newark, CA 94560
- 16 Boeing, El Segundo, CA 90245
- 17 Tesla, Palo Alto, CA 94306
- 18 SpaceX, Hawthorne, CA 90250
- 19 Planet Labs, San Francisco, CA 94107
- 20 NovaSignal, Los Angeles, CA 90064
- 21 Jet Propulsion Laboratory, Pasadena, CA 91109
- 22 Mercedes-Benz Research and Development North America, Long Beach, CA 90810
- 23 Epic Systems Corporation, Verona, WI 53593
- 24 California State Polytechnic University, Pomona, CA 91768
- 25 Economics Department, University of California, Los Angeles, CA 90095
- 26 Experior Laboratories, Oxnard, CA 93033
- 27 Qualcomm, San Diego, CA 92121

*Correspondence to: vassilis@ucla.edu

49 **Summary paragraph:**

50 In near-Earth space, the magnetosphere, energetic electrons (tens to thousands of kiloelectron
51 volts) orbit around Earth, forming the radiation belts. When scattered by magnetospheric
52 processes, these electrons precipitate to the upper atmosphere, where they deplete ozone, a
53 radiatively active gas, modifying global atmospheric circulation. Relativistic electrons (those
54 above a few hundred kiloelectron volts), can reach the lowest altitudes and have the strongest
55 effects on the upper atmosphere; their loss from the magnetosphere is also important for
56 space weather. Previous models have only considered magnetospheric scattering and
57 precipitation of energetic electrons; atmospheric scattering of such electrons has not been
58 adequately considered, principally due to lack of observations. Here we report the first
59 observations of this process. We find that atmospherically-scattered energetic (relativistic)
60 electrons form a low-intensity, persistent “drizzle”, whose integrated energy flux is comparable
61 to (greater than) that of the more intense but ephemeral precipitation by magnetospheric
62 scattering. Thus, atmospheric scattering of energetic electrons is important for global
63 atmospheric circulation, radiation belt flux evolution, and the repopulation of the
64 magnetosphere with lower-energy, secondary electrons.

65 **Main article:** Polar ozone exerts strong radiative forcing on global atmospheric
66 circulation by modifying temperature, winds, and waves in the upper atmosphere. Energetic
67 electrons from near-Earth space can reach the high-latitude mesosphere (50-100km), where
68 they produce reactive odd nitrogen and hydrogen (NO_x and HO_x), ozone-destroying catalysts.
69 Nitrogen oxides can also descend to the stratosphere (25-50km), where they become the most
70 important contributors to catalytic ozone destruction. Thus, energetic electron precipitation

71 can affect the global ozone cycle^{1,2,3} and global circulation significantly. Despite their
 72 importance for modeling atmospheric circulation, energetic particles have not been adequately
 73 incorporated into global atmospheric models^{4,5,6}, resulting in large discrepancies between
 74 model predictions and observations of vertical ozone profiles⁷. Magnetospheric energetic
 75 electrons (especially relativistic ones) are also important for space weather, as they can damage
 76 satellites and harm astronauts, particularly during magnetic storms^{8,9}. Their fluxes, a delicate
 77 balance of large contributions from transport, acceleration, and loss, vary so as to defy
 78 predictability by modeling. These electrons can be trapped for hours to weeks in the outer
 79 radiation belt, which is near the magnetic equator at geocentric distances of $L=3-7$ Earth radii.
 80 Plasma waves¹⁰ or extreme equatorial field-line curvature¹¹ can scatter them, reducing their
 81 velocity angle (pitch angle, α) relative to the magnetic field, \mathbf{B} , to less than the loss cone angle
 82 ($\alpha < \alpha_{LC}$). This allows them to reach the mesosphere or stratosphere, where they collide, deposit
 83 their energy and are lost from the magnetosphere. Although magnetospheric scattering has
 84 been incorporated into radiation belt diffusion models^{12,13}, because of lack of observations,
 85 atmospheric scattering has not, resulting in significant model deficiencies^{14,15}. Using the first
 86 low-altitude ($\sim 410\text{km}$), high-resolution (in both pitch angle and energy) observations of
 87 energetic (50-5800keV) electrons by the ELFIN mission¹⁶, we report on atmospheric scattering
 88 and its dependence on activity and location. We interpret upgoing electrons ($180^\circ - \alpha_{LC} < \alpha$) at
 89 some energy, E , as secondary electrons produced by atmospheric scattering of either trapped
 90 ($\alpha \sim 90^\circ$) or precipitating ($\alpha < \alpha_{LC}$) primary electrons of a greater energy. (Note: unless otherwise
 91 stated, pitch angles are referenced to the northern hemisphere; for the southern hemisphere,
 92 use their supplementary). We find that the net energetic (relativistic) electron energy flux

precipitation from atmospheric scattering is comparable to (greater than) that from magnetospheric scattering.

ELFIN, a dual CubeSat, polar-orbiting mission launched in 2018, has collected data from >1000 science zones (magnetically mapping to $L=2-15$), covering all local times and a wide range of geomagnetic conditions. We use energetic particle detector instrument (EPDE) data obtained by ELFIN-A (EL-A) from magnetic local times within ± 4 hours of the noon-midnight plane between 2019/09/01 2020/11/13 (~ 700 science zones). The instrument has a single square-aperture field-of-view ($FOV=22^\circ$). Spinning on a plane containing \mathbf{B} , once per spin (~ 3 sec) it provides 15 energy channels (50keV-5800keV) of width $\Delta E/E \sim 40\%$ and 16 spin-phase sectors of width $SCW=22.5^\circ$. Spin-phases are transformed to pitch-angles using the international geophysical reference field (IGRF) model. At ELFIN's altitude, the loss cone is $\alpha_{LC} \sim 67^\circ \pm 2^\circ$. Precipitating (downgoing) or atmospherically-scattered (upgoing) electrons were measured when the detector's full width ($FOV+SCW$) was entirely within the loss cone or the anti-loss cone, respectively. Trapped electrons had sector centers $\alpha=90^\circ \pm 11.25^\circ$.

Atmospheric scattering of precipitating electrons ("backscatter") should produce low upgoing-to-downgoing ratios¹⁵. Thus, when magnetospherically scattered precipitation is significant (relative to trapped fluxes), atmospheric backscatter should yield low upgoing-to-downgoing flux ratios. Atmospheric scattering of (barely) trapped electrons should result in low (relative to trapped) but balanced upgoing and downgoing fluxes at upper atmospheric altitudes (upgoing-to-downgoing ratios $\sim 100\%$). Thus, when magnetospherically-scattered precipitation (and, consequently, its atmospheric backscattering) is low, atmospheric scattering

of trapped fluxes can dominate, resulting in upgoing-to-downgoing flux ratios $\sim 100\%$ *at the upper atmosphere*. Under such conditions, the absence of magnetospheric scattering sites near the equator should allow atmospherically-scattered upgoing energetic electrons from the opposite hemisphere to be detected at the local hemisphere as downgoing, resulting in upgoing-to-downgoing ratios $\sim 100\%$ *also at the satellite*.

ELFIN-A observations of a northern, nightside (MLT ~ 1) science zone (Figure 1a) during an active time (the D_{ST} index¹⁷ had a minimum of -49nT fourteen hours earlier¹⁸) confirms the above expectations from atmospheric scattering. Significant downgoing fluxes ($\alpha < \alpha_{LC}$) are evident between $L=3.5$ and 6.5 (Figure 1b-c). When the downgoing energy flux (precipitation) was a large fraction of the trapped flux (as between 13:13:00 and 13:15:00UT, Figure 1f,h), the upgoing ($180^\circ - \alpha_{LC} < \alpha$) flux intensified, too (Figure 1d), but remained lower than the precipitation (upgoing-to-downgoing ratio was a few percent, Figure 1i). Conversely, when the precipitation was low, only a few percent of the trapped flux (as between 13:11:50 and 13:12:20UT, Figure 1f,h), the upgoing flux was also low (Figure 1d), but comparable to the precipitation (up-to-down flux ratio $\sim 100\%$, Figure 1i).

When intense precipitation from magnetospheric scattering occurs up to some maximum energy, E_{pmax} , atmospheric scattering above E_{pmax} is expected continue to be dominated by atmospheric electron scattering at both hemispheres (upgoing-to-downgoing ratio $\sim 100\%$), impervious to magnetospheric scattering and its atmospheric feedback below E_{pmax} . Indeed, this can be seen at $\sim 13:12:35\text{UT}$, when the downgoing-to-perpendicular ratio (Figure 1h) was elevated ($\sim 50\%$) at $E < E_{pmax} \sim 500\text{keV}$: while the upgoing-to-downgoing ratio (Figure 1i) was suppressed ($\sim 30\%$) at $E < E_{pmax}$, it remained $\sim 100\%$ at $E > E_{pmax}$. Subsequently, as

E_{pmax} increased progressively from 150keV to 800keV (13:12:45-13:13:15UT, Figure 1h), the energy where the upgoing-to-downgoing ratio transitioned from low (<10%) to high (>60%) values followed E_{pmax} (Figure 1i), as expected. Additional examples are shown in Extended Data Figures 1 and 2 (nightside and dayside, respectively). Therefore, atmospheric scattering of trapped fluxes is quantifiable and long-lasting, based on case studies.

Atmospheric scattering of intense, high-energy precipitation is also expected to create copious backscattered electrons at $E \ll E_{\text{pmax}}$. Indeed, at 13:13:10–13:14:00UT, when the downgoing-to-perpendicular ratio is high, $\sim 100\%$, with $E_{\text{pmax}} \sim 1\text{MeV}$ (Figure 1h), the upgoing-to-downgoing flux ratios are low ($\sim 1\text{-}2\%$) near E_{pmax} (Figure 1i), but are significant (20-50%) at energies several times lower than E_{pmax} (50-150keV). Another example is in Extended Data Figure 1 (13:47:15–13:47:30UT). Thus, atmospheric scattering of precipitation can also be a significant source of energetic electrons in the magnetosphere, as previously suggested^{14,15}.

Henceforth we refer to atmospheric scattering of trapped fluxes (upward or downward) as “energetic electron drizzle” and to atmospheric scattering of magnetospheric precipitation (upward only) as “energetic electron backscatter”. Upgoing secondary electrons can be produced by either (generally both). Likewise, downgoing (or “precipitating”) energetic electrons can be from either downward drizzle (even from the opposite hemisphere) or magnetospheric precipitation (originating from magnetospheric scattering even after subsequent backscatter at the opposite hemisphere).

To further quantify the importance of atmospheric scattering, we employ broad-energy flux channels LoE (50-430keV) and HiE (430-5800keV) in the upgoing, downgoing and

perpendicular directions (f_u , f_d , f_{\perp} , respectively), and statistically significant flux ratios within each channel RLoE, RHIE (f_u/f_d , f_d/f_{\perp} , f_u/f_{\perp} , with relative error <50%), as in Figure 1j-m (and Extended Data Figures 1l-L, 2l-L). These form the basis of our statistical analysis, below. (Materials and Methods and Extended Data Figure 3 detail how these were constructed).

Medians of the above ratios at the nightside (Figure 2b,d) exhibit L-shell variations familiar from the nightside time series examined previously (Figure 1; Extended Data Figure 1): at low L-shells, atmospheric drizzle dominates (f_d/f_{\perp} <10%; f_u/f_d ~70-100%); at high L-shells, magnetospheric precipitation dominates (f_d/f_{\perp} >40%; f_u/f_d ~10%). The transition L-shell decreases with geomagnetic activity (based on the Auroral Electrojet index $AE^{17,18}$). This is consistent with an equatorward motion of the equatorward edge of the auroral oval (where intense plasma waves and field-line scattering sites responsible for magnetospheric scattering map), typical during active times¹⁹. At the dayside (Figure 2a,c), precipitation is dominated by drizzle (as in Extended Data Figure 2). The statistical behavior of our dataset is thus expected to be bimodal, with a drizzle-dominated subset at low L-shells and a magnetospheric precipitation-dominated subset at high L-shells.

And, indeed, probability density functions (PDFs) in $(f_d+f_u)/f_{\perp}$ -space (Figure 3a) reveal two peaks: The low-precipitation PDF peak ($(f_d+f_u)/f_{\perp}$ ~2-10%) has f_u/f_d ~100%, corresponds to the low L-shells in Figures 1 and 2 (also Extended Data Figures 1 and 2), and is identified as atmospheric drizzle. The high-precipitation PDF peak ($(f_d+f_u)/f_{\perp}$ ~100%) has f_u/f_d ~7±3%, corresponds to the high L-shells in the above figures, and is identified as enhanced precipitation mostly due to magnetospheric scattering.

Precipitation of 50-430keV (LoE) electrons (Figure 3c) is dominated by intense magnetospheric scattering (mostly by plasma waves), which overcomes the more common but lower-intensity drizzle. Precipitation of 430-5800keV (HiE) and 50-5800keV (integral channel) electrons is also dominated by magnetospheric scattering, but exhibits a significant contribution from drizzle. Upgoing fluxes also exhibit a similar bimodal behavior (Figure 3b). At all channels (LoE, HiE and integral), the drizzle peak ($(f_d+f_u)/f_{\perp} \sim 2-10\%$) dominates the upgoing flux. However, the magnetospheric precipitation peak ($(f_d+f_u)/f_{\perp} \sim 100\%$), corresponding mostly to backscatter (though likely some upward drizzle, too), also contributes significantly to the LoE channel. These peaks and their properties remain similar when examined as a function of f_{\perp} (Extended Data Figure 4) and geomagnetic activity and for the subset of the outer radiation belt ($3 < L < 7$).

Evaluation of atmospheric scattering's net impact on precipitation starts from Table 1, showing the measured upgoing-to-downgoing flux ratios, $r = \langle f_u \rangle / \langle f_d \rangle$, separately for the nightside, dayside and combined. We see that $r \sim 45\%$ for HiE and $r \sim 18\%$ for the integral channel.

Next, we recall that the downgoing flux contribution from scattering below the satellite cannot be measured directly; it must be inferred. We note that the upgoing HiE and integral flux (Figure 3b) are dominated by upward drizzle, f_a (main peak, and likely a good part of the secondary peak), which is up-down symmetric and occurs at both atmospheric feet of a field line. It is therefore a good proxy for the downward drizzle arriving from the opposite hemisphere. The measured downgoing flux for the HiE and integral channels (Figure 3c) is

199 supplied by both magnetospheric precipitation, f_m , and downward drizzle from the opposite
 200 hemisphere, f_a . Thus, at ELFIN, to zero order, we measure (Table 1): $r = \langle f_u \rangle / \langle f_d \rangle \sim f_a / (f_a + f_m)$. The
 201 atmospheric scattering contribution to precipitation is $\sim 2f_a$, the total precipitation at each
 202 hemisphere is $\sim 2f_a + f_m$, and the relative contribution of atmospheric scattering to precipitation
 203 is $R = 2f_a / (2f_a + f_m)$. If $x = 2f_a / f_m$ (atmospheric relative to magnetospheric scattering), using $r = x / (x + 2)$
 204 and the measured values of r (Table 1), we find $x = 161\%$, $R = 1 / (1 + x) \sim 62\%$ for HiE, and $x \sim 45\%$,
 205 $R \sim 31\%$ for the integral channel. For the outer radiation belt ($3 < L < 7$) during all activity levels and
 206 during only active times ($D_{ST} < -20\text{nT}$), we obtain (Extended Data Table 1) similar values, though
 207 somewhat reduced due to the increased relative contribution of magnetospheric precipitation
 208 in those subsets.

209 Thus, atmospheric scattering contributes more than magnetospheric scattering to the
 210 precipitation energy at relativistic energies ($>430\text{keV}$) and as much as 45% of the
 211 magnetospheric precipitation at energies $>50\text{keV}$. Since relativistic electrons can reach the
 212 upper/middle stratosphere, resulting in very efficient catalytic ozone depletions, and are also a
 213 critical contributor to space weather, our results necessitate a factor of ~ 2 upwards revision of
 214 energy flux inputs in atmospheric models and energy flux losses in radiation belt models.
 215 Moreover, during intense magnetospheric precipitation, the backscattered energetic electron
 216 energy flux at low energies is a significant fraction of both precipitating and trapped flux. Thus,
 217 atmospheric scattering can be also important for seeding the radiation belts with electrons and
 218 for generating plasma waves; its effects need to be further quantified with observationally-
 219 driven modeling.

221 **Data availability statement**

222 ELFIN data are available through <http://elfin.igpp.ucla.edu>.

223 **Code availability statement**

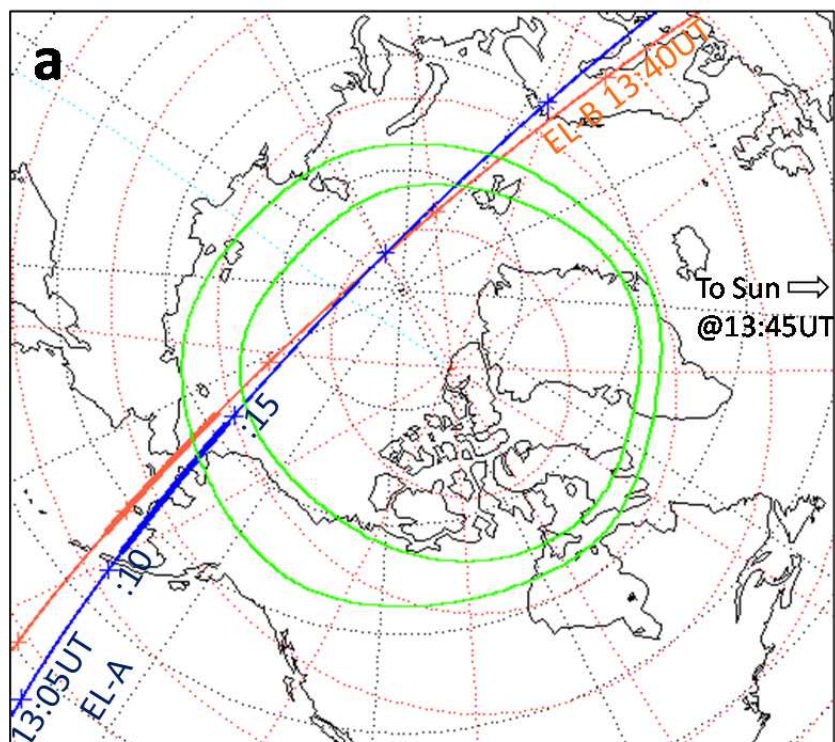
224 ELFIN mission data have been imported, analyzed, and plotted using corresponding
225 plug-ins to the open-source SPEDAS analysis platform²⁰ (<http://spedas.org>).

226

Supplementary Information is linked to the online version of the paper at www.nature.com/nature.

Acknowledgments: We acknowledge support by NASA award NNX14AN68G (5/22/2014 – present) and NSF awards # AGS-1242918 (9/24/2014-7/31/2019) and AGS-2019950 (July 2020 – present). We are grateful to NASA’s CubeSat Launch Initiative program for successfully launching the ELFIN satellites in the desired orbits under ELaNa XVIII. We thank the AFOSR for early support of the ELFIN program under its University Nanosat Program, UNP-8 project, contract # FA9453-12-D-0285 (02/01/2013-01/31/2015). We also thank the California Space Grant program for student support during the project’s inception (2010-2014). We acknowledge the hardware contributions and technical assistance of Mr. David Hinkley and The Aerospace Corporation. We thank V. A. Sergeev, Y. A. Shprits and W. Greer for useful discussions in the early stages of the program. We acknowledge the critical contributions of the many volunteer ELFIN team members (more than 250 students). We thank Ms. J. Hohl for editorial assistance with the manuscript.

244 **Figure 1a**



245

246

Figure 1b-m

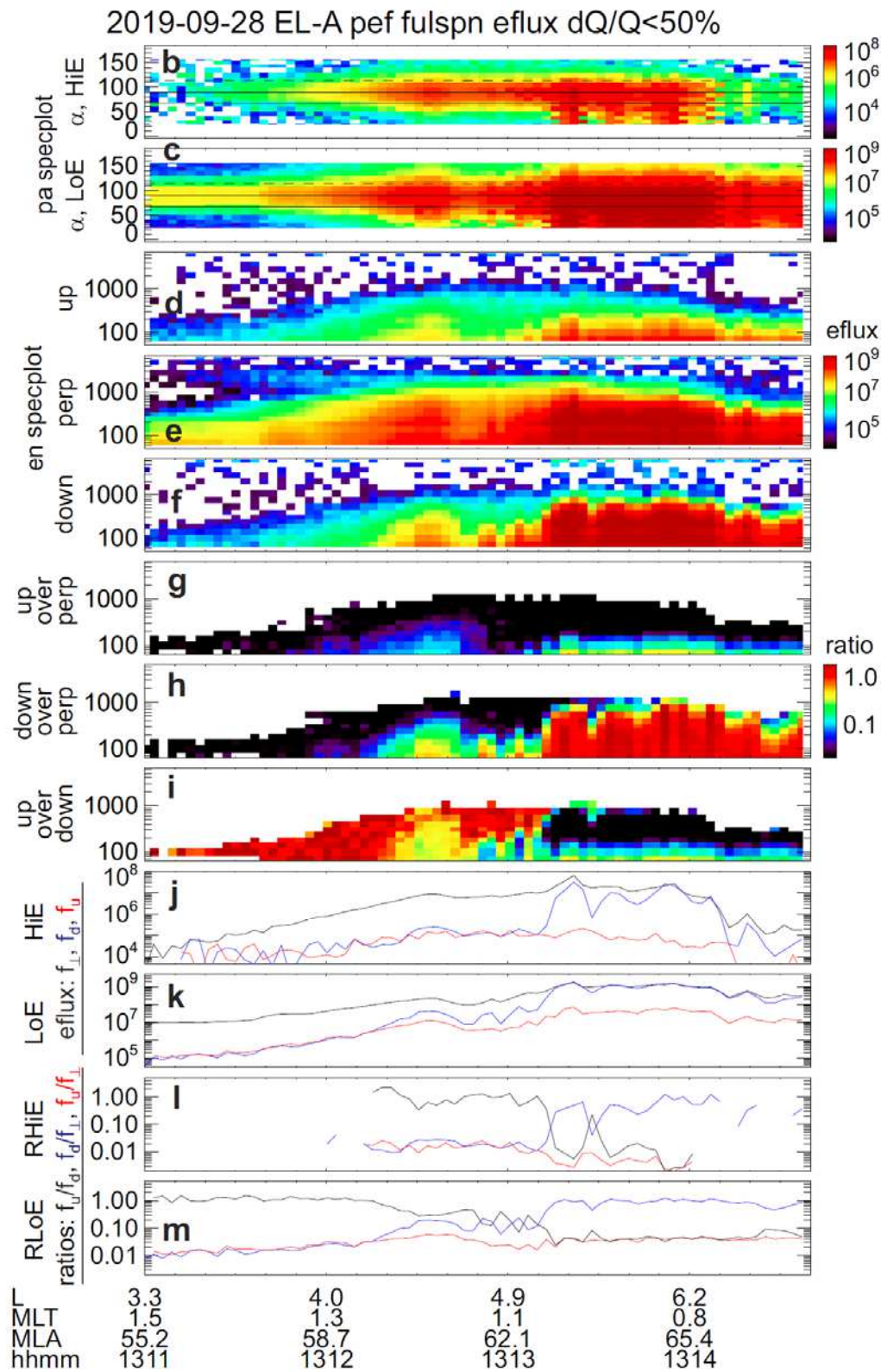
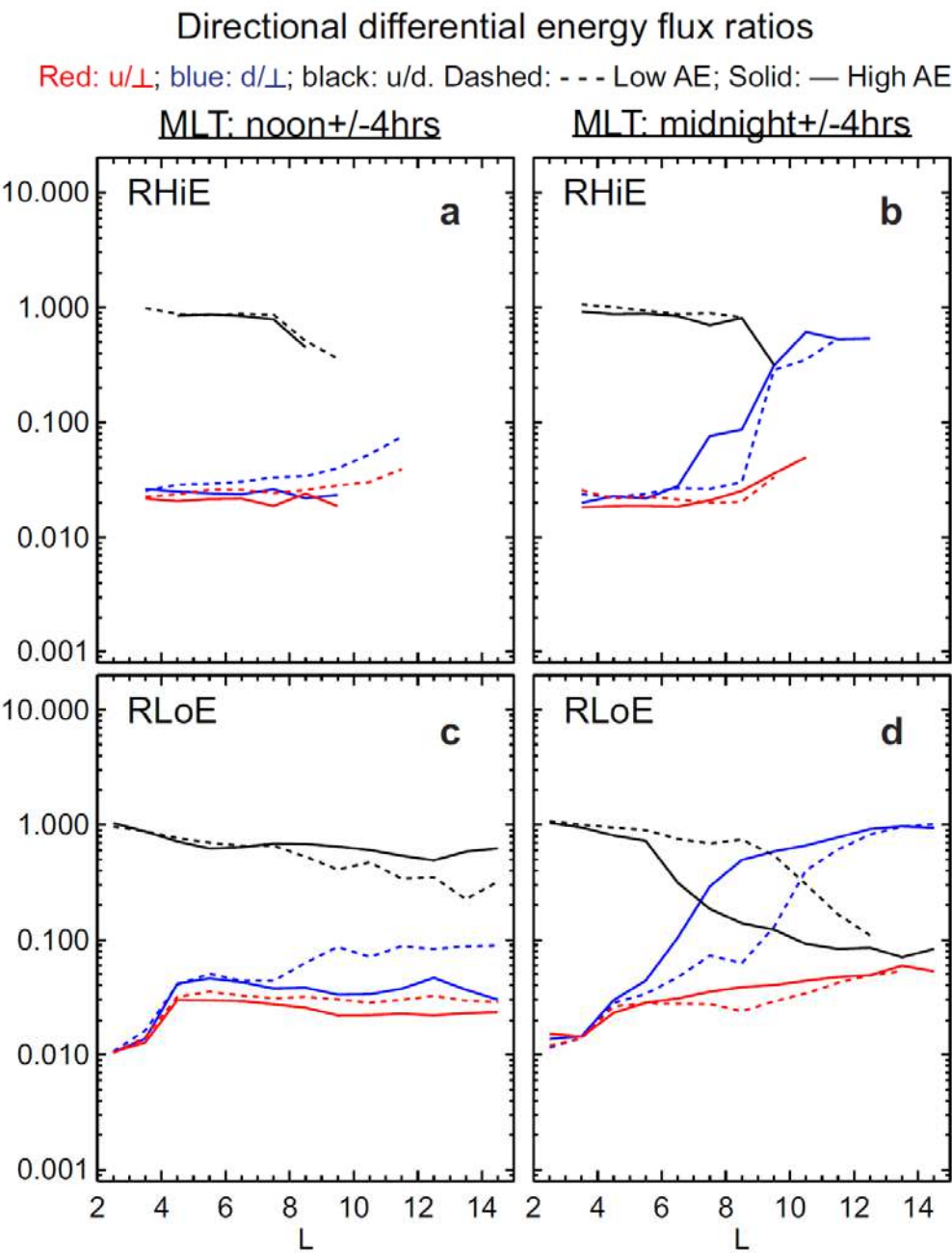


Figure 1 | ELFIN storm-time, nightside crossing of the outer radiation belt and auroral zone.

(a) EL-A satellite track geographic projections (fixed at 13:45UT) on 28 September 2019. Thick lines represent times of data capture; 5-min intervals are indicated by crosses. Black (red) dotted lines are geographic (corrected geomagnetic) meridians and parallels. Green lines are nominal auroral oval boundaries. (b-c) Pitch-angle spectrograms of differential directional energy flux (“energy flux” in $\text{keV}/\text{cm}^2\text{s str MeV}$) in broad-energy electron channels HiE and LoE (430-5800keV and 50-430keV energies, respectively). Bottom solid and upper dashed horizontal lines in each spectrogram mark the loss cone ($\alpha=\alpha_{LC}$) and anti-loss cone ($\alpha=180^\circ-\alpha_{LC}$); middle solid line denotes $\alpha=90^\circ$. (d-f) Energy-time spectrograms of upgoing (within anti-loss cone: $\alpha>180^\circ-\alpha_{LC}$), nearly-perpendicular to **B** (trapped), and downgoing (within loss cone: $\alpha<\alpha_{LC}$) electron energy flux. The energy ranges from 50keV to ~5800keV. (g-i) Energy-time spectrograms of upgoing-to-perpendicular (up-to-perp, f_u/f_\perp), downgoing-to-perpendicular (down-to-perp, f_d/f_\perp), and upgoing-to-downgoing (f_u/f_d) electron energy flux. (j-k) Energy flux in channels HiE and LoE (black: f_\perp ; blue: f_d ; red: f_u). (l-m) Ratios of energy flux in channels HiE and LoE, respectively (black: f_u/f_d ; blue: f_d/f_\perp ; red: f_u/f_\perp). Annotations denote L-shell (L), dipole magnetic local time (MLT), dipole magnetic latitude (MLA) and Universal Time (UT).



269

270

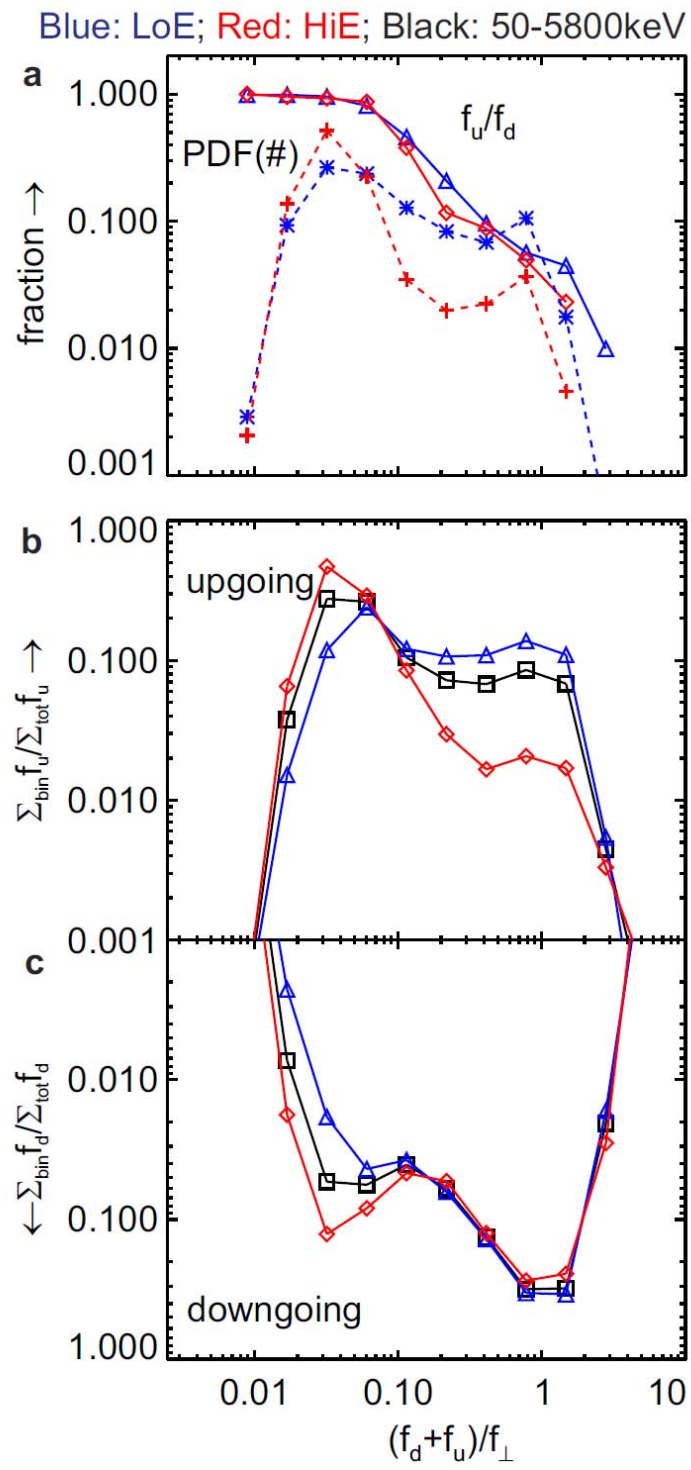
271 **Figure 2 | Dependence of energy flux ratios on L-shell, local time, and activity.**

272 **(a-d)** Medians of ratios: f_u/f_{\perp} (red), f_d/f_{\perp} (blue), f_u/f_d (black) as a function of L-shell. Top and
273 bottom panels: I430 and I50 energy channels, respectively. Left and right panels: dayside and
274 nightside, respectively. Dashed and solid lines: data correspond to below and above the median
275 AE, respectively. (AE medians for dayside and nightside databases are: 110nT and 160nT,
276 respectively).

277

278

279 **Figure 3**



280

281

Figure 3 | Distribution of data, fluxes, and flux ratios as a function of loss-cone flux.

(a) Probability density functions of all data in the I50 and I430 channels (blue stars and red crosses, respectively) and medians of flux ratios (f_u/f_d) for these channels (blue triangles and red diamonds, respectively). **(b)** Relative contribution to net upward flux within the I50 and I430 broad differential broad energy channels (blue triangles and red diamonds, respectively) and within the summed energy channel representing the total energy flux measured by the detector, i.e., at energies 50 keV – 5.8 MeV (black squares). **(c)** Same as in **(b)** but for the downward flux. Two-dimensional versions of several of these distributions, also plotted against the perpendicular energy flux, are shown in Extended Data Figure 4.

Table 1

Average Directional Electron Fluxes [†] and their Measured Ratios (all data, 2<L<15)							
MLT	Energy [keV]	$r = \langle f_u \rangle / \langle f_d \rangle$	$\langle f_d \rangle / \langle f_{\perp} \rangle$	$\langle f_{\perp} \rangle$ [Units]	keV/cm ² s str MeV (Differential Directional Energy Flux)	Inferred [‡] Ratios	
Night	LoE: 50-430	9.4%	39.1%	1.28E+07		$x = 2f_a/f_m$	$R = 2f_a/(2f_a + f_m)$
	HiE: 430-5800	36.9%	9.8%	1.17E+06			
Day	LoE: 50-430	14.2%	25.1%	6.96E+06			
	HiE: 430-5800	80.3%	6.1%	4.11E+05			
Night+Day, Residence-time Norm'ed	LoE: 50-430	10.6%	34.2%	9.88E+06			
	HiE: 430-5800	44.7%	8.9%	7.89E+05		161%	62%
	50-5800 (Integral)	18.3%	20.8%	7.99E+06 keV/cm ² s str		45%	31%

[†]Noise subtracted: $f_{n,HiE} = 3.48 \cdot 10^3$, $f_{n,LoE} = 2.74 \cdot 10^3$ [keV/cm² s str MeV]

[‡]where $R = x/(x+1)$; $r = x/(x+2)$

Table 1 | Differential and integral directional energy fluxes and ratios under all geomagnetic conditions, local times and latitudes in our database (2<L<15). Ratios of time averages rather than medians of ratios have been used, to accurately characterize total energy flux ratios. Night+Day ratios were computed directly from the numbers above them, assuming equal satellite residence time at day and night. Bottom row, which represents the integral directional energy flux channel (50-5800keV), was computed directly from the rows above it. f_u and f_d are upgoing and downgoing fluxes, $\langle \rangle$ represents average, and f_a and f_m are the measured contributions to precipitation from atmospheric scattering and magnetospheric scattering. The ratios x and R are the inferred net contributions to precipitation from atmospheric scattering relative to magnetospheric scattering and relative to the total precipitation, respectively.

306 **Supplementary Information:**

307 Methods

308 Extended Data Figures 1 - 4

309 Extended Data Table 1

310

311

312

- ¹ Jackman, C. H., Frederick, J.E. & Stolarski, R.S. Production of odd nitrogen in the stratosphere and mesosphere: An intercomparison of source strengths. *J. Geophys. Res., Oceans*. **85**, C12, 7495-7505 <https://doi.org/10.1029/JC085iC12p07495> (1980).
- ² Thorne, R.M. The importance of energetic particle precipitation on the chemical composition of the middle atmosphere. *PAGEOPH* **118**, 128–151 <https://doi.org/10.1007/BF01586448> (1980).
- ³ Randall, C.E. et al. Stratospheric effects of energetic particle precipitation in 2003–2004. *Geophys. Res. Lett.* **32**, 5, <https://doi.org/10.1029/2004GL022003> (2005).
- ⁴ Baker, D.N. et al. Highly relativistic magnetospheric electrons: A role in coupling to the middle atmosphere? *Geophys. Res. Lett.* **14**, 10 <https://doi.org/10.1029/GL014i010p01027> (1987).
- ⁵ Mirinova, I. A. et al. Ionization of the Polar Atmosphere by Energetic Electron Precipitation Retrieved From Balloon Measurements. *Geophys. Res. Lett.* **46**, 2, 990-996 <https://doi.org/10.1029/2018GL079421> (2019).
- ⁶ Funke, B. et al. HEPPA-II model–measurement intercomparison project: EPP indirect effects during the dynamically perturbed NH winter 2008–2009. *Atmos. Chem. Phys.*, **17**, 5, 3573–3604 <https://doi.org/10.5194/acp-17-3573-2017> (2017).
- ⁷ Randall, C.E. et al. Simulation of energetic particle precipitation effects during the 2003–2004 Arctic winter. *J. Geophys. Res. Space Phys.* **120**, 6, 5035-504 <https://doi.org/10.1002/2015JA021196> (2016).
- ⁸ Gonzales, W.D. et al. What is a geomagnetic storm? *J. Geophys. Res.* **99**, A4, 5771-5792 [doi:10.1029/93JA02867](https://doi.org/10.1029/93JA02867) (1994).
- ⁹ Baker, D. N., et al., Space Weather Effects in the Earth’s Radiation Belts, *Space Sci. Rev.*, **214**, 17, <https://doi.org/10.1007/s11214-017-0452-7> (2018).
- ¹⁰ Schulz, M. & Lanzerotti, L.J. Particle Diffusion in the Radiation Belts in Physics and Chemistry in Space (ed. vol. 7, Roederer, J.G.)(Springer-Verlag, New York) <https://doi.org/10.1007/978-3-642-65675-0> (1974).
- ¹¹ Imhof, W.L., Reagan, J.B. & Gaines, E.E., Fine-scale spatial structure in the pitch angle distributions of energetic particles near the midnight trapping boundary. *J. Geophys. Res. Space Phys.* **82**, 32, 5215-5221 <https://doi.org/10.1029/JA082i032p05215> (1977).
- ¹² Shprits, Y.Y., Subbotin, D. & Binbin, N., Evolution of electron fluxes in the outer radiation belt computed with the VERB code. *J. Geophys. Res., Space Phys.* **114**, A11 <https://doi.org/10.1029/2008JA013784> (2009).
- ¹³ Glauert, S. A., Horne, R.B., & Meredith, N.P. Three-dimensional electron radiation belt simulations using the BAS Radiation Belt Model with new diffusion models for chorus, plasmaspheric hiss, and lightning-generated whistlers. *J. Geophys. Res., Space Phys.*, **119**, 1, 268-289 <https://doi.org/10.1002/2013JA019281> (2014).
- ¹⁴ Khazanov, G. V., Glocer, A. & Chu, M. The Formation of Electron Heat Flux in the Region of Diffuse Aurora. *J. Geophys. Res., Space Phys.* **125**, 8, <https://doi.org/10.1029/2020JA028175> (2020).

-
- ¹⁵ Marshall, R. A., & Bortnik, J. Pitch Angle Dependence of Energetic Electron Precipitation: Energy Deposition, Backscatter, and the Bounce Loss Cone. *J. Geophys. Res., Space Phys.* **123**, 3, 2412-2423
<https://agupubs.onlinelibrary.wiley.com/doi/full/10.1002/2017JA024873> (2018).
- ¹⁶ Angelopoulos, V., et al. The ELFIN Mission, *Space Sci. Rev.* **216**, 103
<https://doi.org/10.1007/s11214-020-00721-7> (2020).
- ¹⁷ Mayaud, P. N. Derivation, meaning, and use of geomagnetic indices. *Geophys. Monogr. Ser.* **22**, 154 pp., American Geophysical Union, doi:[10.1029/GM022](https://doi.org/10.1029/GM022) (1980).
- ¹⁸ <http://wdc.kugi.kyoto-u.ac.jp/>
- ¹⁹ Yokoyama, N., Kamide, Y., & Miyaoka, H., The size of the auroral belt during magnetic storms. *Ann. Geophys.* **16**, 566-573 <https://doi.org/10.1007/s00585-998-0566-z> (1998).
- ²⁰ Angelopoulos, V., et al., The Space Physics Environment Data Analysis System (SPEDAS). *Space Sci. Rev.* **215**, 9 <https://doi.org/10.1007/s11214-018-0576-4> (2019).

Supplementary Materials for:

Atmospheric scattering of energetic electrons from near-Earth space

V. Angelopoulos^{1*}, E. Tsai¹, C. Wilkins¹, X.-J. Zhang¹, A. V. Artemyev¹, J. Liu¹, A. Runov¹, L. Iglesias¹, D. L. Turner², R. J. Strangeway¹, R. E. Wirz³, W. Li⁴, L. Adair^{1,5}, R. P. Caron¹, M. Chung², P. Cruce⁶, E. Grimes¹, K. Hector⁷, M. J. Lawson¹, D. Leneman¹, E. V. Masongsong¹, A. Norris¹, C. L. Russell¹, C. Shaffer⁸, J. Wu¹, S. Jha^{1,9}, J. King^{1,9}, S. Kumar^{1,10}, K. Nguyen^{1,3}, M. Nguyen^{1,11}, A. Palla^{1,9}, A. Roosnovo^{1,10}, E. Xie^{1,11}, R. Yap^{1,12}, C. Young^{1,9}, J. B. Blake¹³, N. Adair⁵, M. Allen¹⁴, M. Anderson¹⁵, M. Arreola-Zamora^{1,14}, J. Artinger^{1,10}, J. Asher², D. Branchevsky¹³, M. R. Capitelli⁵, R. Castro^{7,9}, G. Chao^{3,16}, N. Chung¹⁷, M. Cliffe¹⁸, K. Colton¹⁹, C. Costello²⁰, D. Depe¹¹, B. W. Domae¹¹, S. Eldin¹¹, L. Fitzgibbon⁸, A. Flemming¹⁴, I. Fox³, D. M. Frederick⁵, A. Gilbert¹¹, A. Gildemeister¹⁴, A. Gonzalez⁹, B. Hesford²¹, R. Krieger²², K. Lian¹⁴, J. Mao²³, E. McKinney²⁴, J. P. Miller⁹, M. Nuesca⁹, E. S. Y. Park²⁵, C. E. Pedersen³, Z. Qu³, R. Rozario¹⁸, E. Rye¹¹, R. Seaton¹, A. Subramanian¹⁴, S. R. Sundin⁸, A. Tan²⁶, W. Turner¹⁰, A. J. Villegas¹⁰, M. Wasden³, G. Wing⁹, C. Wong¹⁰, A. Zarifian²¹, G. Y. Zhang²⁷

Affiliations:

- 1 Earth, Planetary, and Space Sciences Department, and Institute of Geophysics and Planetary Physics, University of California, Los Angeles, CA 90095
- 2 Johns Hopkins University Applied Physics Laboratory, Laurel, Maryland 20723
- 3 Mechanical and Aerospace Engineering Department, Henry Samueli School of Engineering, University of California, Los Angeles, CA 90095
- 4 Department of Astronomy and Center for Space Physics, Boston University, Boston, MA 02215
- 5 Millenium Space Systems, El Segundo, CA 90245
- 6 Apple Inc., Cupertino, CA 95014
- 7 Raytheon Space and Airborne Systems, El Segundo, CA 90245
- 8 Tyvak Nano-Satellite Systems, Inc., Irvine, CA 92618
- 9 Computer Science Department, Henry Samueli School of Engineering, University of California, Los Angeles, CA 90095
- 10 Physics and Astronomy Department, University of California, Los Angeles, CA 90095
- 11 Electrical and Computer Engineering Department, Henry Samueli School of Engineering, University of California, Los Angeles, CA 90095
- 12 Mathematics Department, University of California, Los Angeles, CA 90095
- 13 The Aerospace Corporation, El Segundo, CA 90245
- 14 Northrop Grumman Aerospace Systems, Redondo Beach, CA 90278
- 15 Lucid Motors, Newark, CA 94560
- 16 Boeing, El Segundo, CA 90245
- 17 Tesla, Palo Alto, CA 94306
- 18 SpaceX, Hawthorne, CA 90250
- 19 Planet Labs, San Francisco, CA 94107
- 20 NovaSignal, Los Angeles, CA 90064
- 21 Jet Propulsion Laboratory, Pasadena, CA 91109
- 22 Mercedes-Benz Research and Development North America, Long Beach, CA 90810
- 23 Epic Systems Corporation, Verona, WI 53593
- 24 California State Polytechnic University, Pomona, CA 91768
- 25 Economics Department, University of California, Los Angeles, CA 90095
- 26 Exporior Laboratories, Oxnard, CA 93033
- 27 Qualcomm, San Diego, CA 92121

*Correspondence to: vassilis@ucla.edu

50 This file includes:

51

52 Methods (pages 3-6)

53 Extended Data Figures 1 – 4 (pages 7-15)

54 Extended Data Table 1 (page 16)

55

56

57

58

59

60

Methods

M1. Statistical significance of loss cone fluxes and their ratios

Although the EPDE's side-penetrating radiation is insignificant thanks to high shielding and coincidence logic¹⁶, counting statistics must still be utilized to guarantee a robust signal-to-noise ratio. Poisson statistics govern detector counts; the relative error dQ/Q of any quantity Q proportional to the count rate (such as the energy flux) is $1/\sqrt{N}$, where N is the total number of counts in the measurement. To determine it, we obtain the net raw number of counts, N , that contributed to each measurement (e.g., Q may be the average energy flux in two or three sectors within the loss cone) and carry this information in the data processing along with the measurement. For derived products, such as integral or average energy flux, we then use error propagation formulas to compute the error for each quantity at every time step. An error tolerance of $dQ/Q < 50\%$ for a data point would thus require that at least $N=4$ counts contributed to that measurement of Q .

Electronic noise, which also exists in the measurements, can be recognized as random, low-flux pixels at high energies in the energy spectra in Figures 1d-f (and also in Extended Data Figures 1C-E and 2C-E). Most often each pixel corresponds to one count. This electronic noise is readily eliminated by the aforementioned criterion $dQ/Q < 50\%$ when applied to derived products, such as flux ratio spectrograms (Figures 1g-i; Extended Data Figures 1F-H and 2F-H), or to the time-series ratios of directional broad-energy channels HiE and LoE. The very low contribution of electronic noise to the measurement can be readily assessed from data collected at the magnetic equator, below the inner belt, when no geophysical signal is present. From such data we determined that electronic noise contributes $f_{n,HiE} = 3.48 \times 10^{-3}$

keV/cm²s·str·MeV and $f_{n,LoE} = 2.74 \times 10^3$ keV/cm²s·str·MeV to the energy flux in the two energy channels, HiE and LoE, respectively. We subtracted this noise from measurements in our statistics if they had not already been subjected to the counting statistics threshold (e.g., $dQ/Q < 50\%$ or similar) that automatically rejects electronic noise.

To demonstrate that noise does not affect our loss-cone measurements, we show in Extended Data Figure 3A the energy flux spectra as a function of pitch angle, averaged over 11 spins during the moderate precipitation interval, 13:12:17-13:12:50 UT in Figure 1. A pitch-angle $\alpha=0^\circ$ corresponds to downgoing electrons, and vertical long-dashed lines denote the loss cone (short-dashed lines denote the anti-loss cone). The dashed colored lines, mirror-images of the downgoing fluxes about the pitch angle, $\alpha=0^\circ$, enable direct comparison of upgoing (solid) and downgoing (dashed) lines at the same energy (color) in the raw data. The upgoing-to-downgoing flux ratio in the loss cone thus can be estimated from Extended Data Figure 3A to be about 30% at low energies (warm colors, higher fluxes) and to approach 100% at high energies (cold colors, lower fluxes). The horizontal dashed line represents a flux corresponding to ~ 10 counts, i.e., a relative error of $dQ/Q \sim 30\%$ (here Q is the energy flux in each sector, centered at one distinct pitch angle). Below that horizontal dashed line, the data points fluctuate considerably, consistent with statistical noise, but above it, the data points vary smoothly in pitch angle. Our conclusions regarding ratio evolution are drawn from fluxes that are well above the horizontal dashed line, based on dQ/Q criteria, and therefore are statistically significant.

Upgoing-to-perpendicular and upgoing-to-downgoing ratios of flux averages derived from Extended Data Figure 3, Panel A, are plotted in Panel C; for convenience, these are plotted

on the left and right halves of the panel, respectively. Only the ratios with $dQ/Q < 30\%$ are plotted; the absolute error based on the number of counts for each ratio is demarcated above and below each point by a vertical bar. This restriction on counting statistics also eliminates electronic noise, as discussed earlier. The upgoing-to-downgoing ratio of the average fluxes (right half of Panel B) exhibits the behavior already surmised from the raw data in Panel A: within the loss cone, it is low at low energies (warm colors) but it approaches 100% at increasing energies (cold colors). This behavior is also consistent with the plots of instantaneous (one per spin) flux ratios in Figure 1i, Figure 1l,m; and their equivalent panels in Extended Figures 1 and 2. It shows that statistical or electronic noise has been duly eliminated and does not interfere with our ability to obtain statistically significant fluxes and flux ratios.

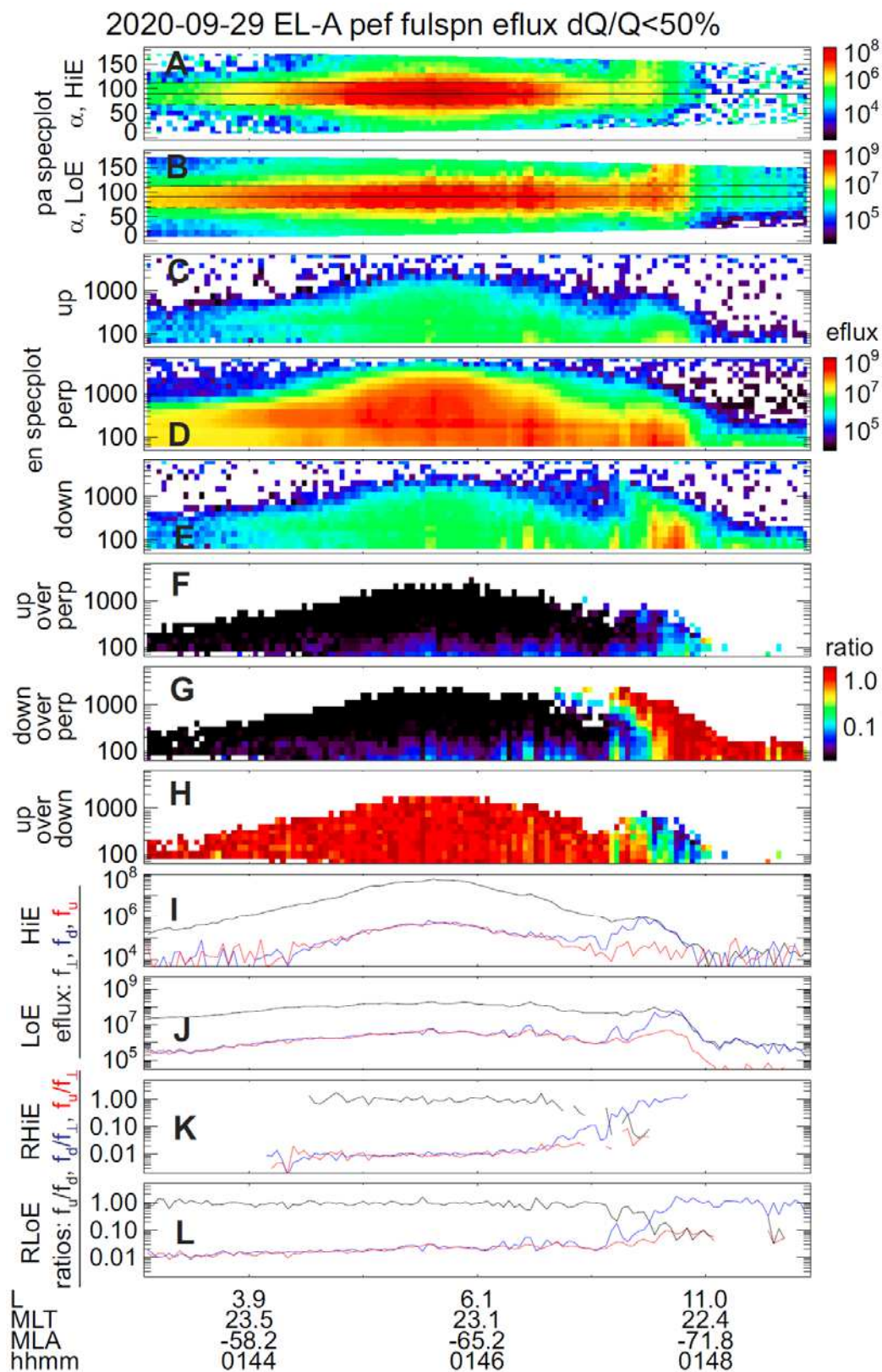
M2. Purity of loss-cone flux

For each sector in spin phase, the detector's finite geometric field of view (22°) and finite accumulation time in spin phase (22.5°) result in a full width of 44.5° and full width at half-max of the contribution to the sector's flux of 33.25° . We rotate the two-dimensional angular detector view (originally in polar and azimuthal angles in spacecraft geometric coordinates) into field-aligned (pitch-angle and gyro-phase) coordinates and collapse it into 1D pitch-angle space at every spin. This results in a smaller full width in pitch-angle space (as low as 22°). We ensure that the viewing windows of the sectors we rely upon to produce the net loss-cone flux are all inside the loss cone, up to the vertices of those windows.

To demonstrate the result of this mapping process, we show the fields of view of all sectors during all spins in Extended Data Figure 3, Panel B (11 spins x 16 sectors are overplotted in that panel, but the spin-to-spin variation is imperceptible, as the magnetic field

128 direction does not change appreciably in the time interval considered). The full width is the thin
129 horizontal line, and the full width half-max is the thick horizontal line. The detector measures
130 particles arriving from the exact edge of the thick line for only 50% of the full sector
131 accumulation time (as opposed to 100% at the center). The contribution to the sector's average
132 flux from pitch angles outside the thick line decreases linearly to 0% at the pitch angles at two
133 edges of the thin line.

134 For a bin's measurements to be counted in the upgoing or downgoing flux, we require
135 that its full width be in the nominal loss cone (or anti-loss cone). Any contribution of the loss
136 cone's finite edge to the total flux is therefore attenuated by the limited time the detector
137 spends in that direction (<1/32 of the sector's flux contribution arises from a 5.6° angle next to
138 its edge) and by the contribution of other sectors well inside the loss cone. In Extended Data
139 Figure 3, Panels B and C, four sectors contribute to the downgoing flux and four to the upgoing
140 flux, the four closest to $\alpha=0^\circ$ and $\alpha=180^\circ$, respectively. Their upgoing-to-perpendicular and
141 upgoing-to-downgoing ratios exhibit a smooth variation with α . Our conclusions on ratios
142 drawn from those four sectors are consistent with the behavior of the two sectors with edges
143 farthest from the loss cone ($>15^\circ$).



146

147 **Extended Data Figure 1 | ELFIN-A nonstorm-time, nightside crossing of the outer radiation**

148 **belt and auroral zone.** Format of Panels A-L is identical to that of Panels b-m in Figure 1. **(A-B)**

149 Pitch-angle spectrograms of differential directional (broad) electron energy flux channels HiE

150 and LoE (430-5800keV and 50-430keV, respectively). Upper solid and bottom dashed horizontal

151 lines: loss cone ($\alpha=\alpha_{LC}$) and anti-loss cone ($\alpha=180^\circ-\alpha_{LC}$); middle solid line: $\alpha=90^\circ$. **(C-E)** Energy-

152 time spectrograms of upgoing, trapped, and downgoing electron energy flux, respectively. **(F-H)**

153 Energy-time spectrograms of upgoing-to-perpendicular (up-to-perp, f_u/f_\perp), downgoing-to-

154 perpendicular (down-to-perp, f_d/f_\perp), and upgoing-to-downgoing (f_u/f_d) electron energy flux,

155 respectively. Note in the f_d/f_\perp spectrogram the clear decrease in the minimum energy of $f_d/f_\perp \sim 1$

156 with increasing latitude, a characteristic signature of precipitation by field-line scattering¹¹. **(I-J)**

157 Energy flux in channels HiE and LoE, respectively (black: f_\perp ; blue: f_d ; red: f_u). **(K-L)** Ratios of

158 energy flux in channels HiE and LoE, respectively (black: f_u/f_d ; blue: f_d/f_\perp ; red: f_u/f_\perp). Annotations

159 denote L-shell (L), dipole magnetic local time (MLT), dipole magnetic latitude (MLA), and

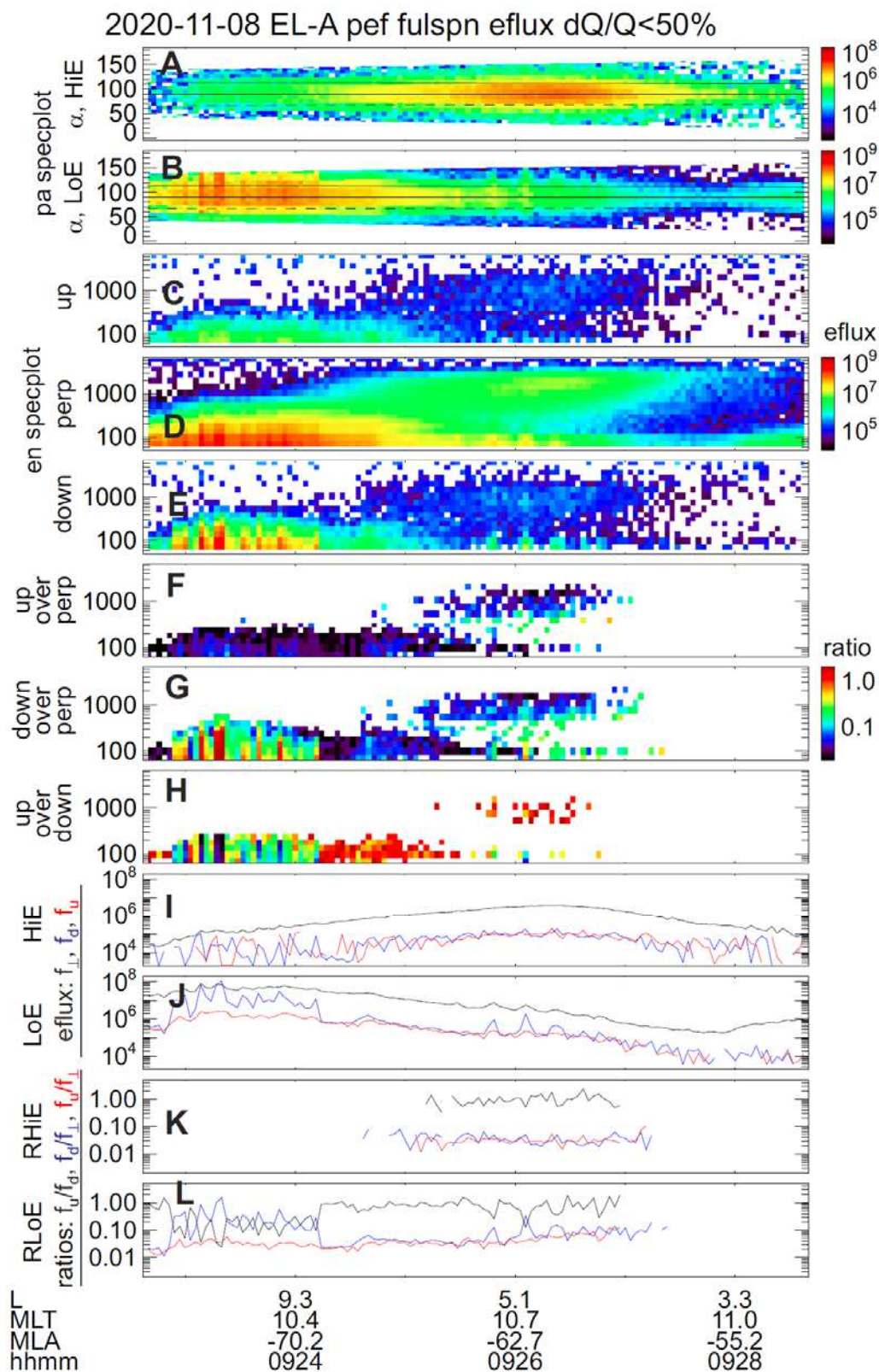
160 Universal Time (UT).

161

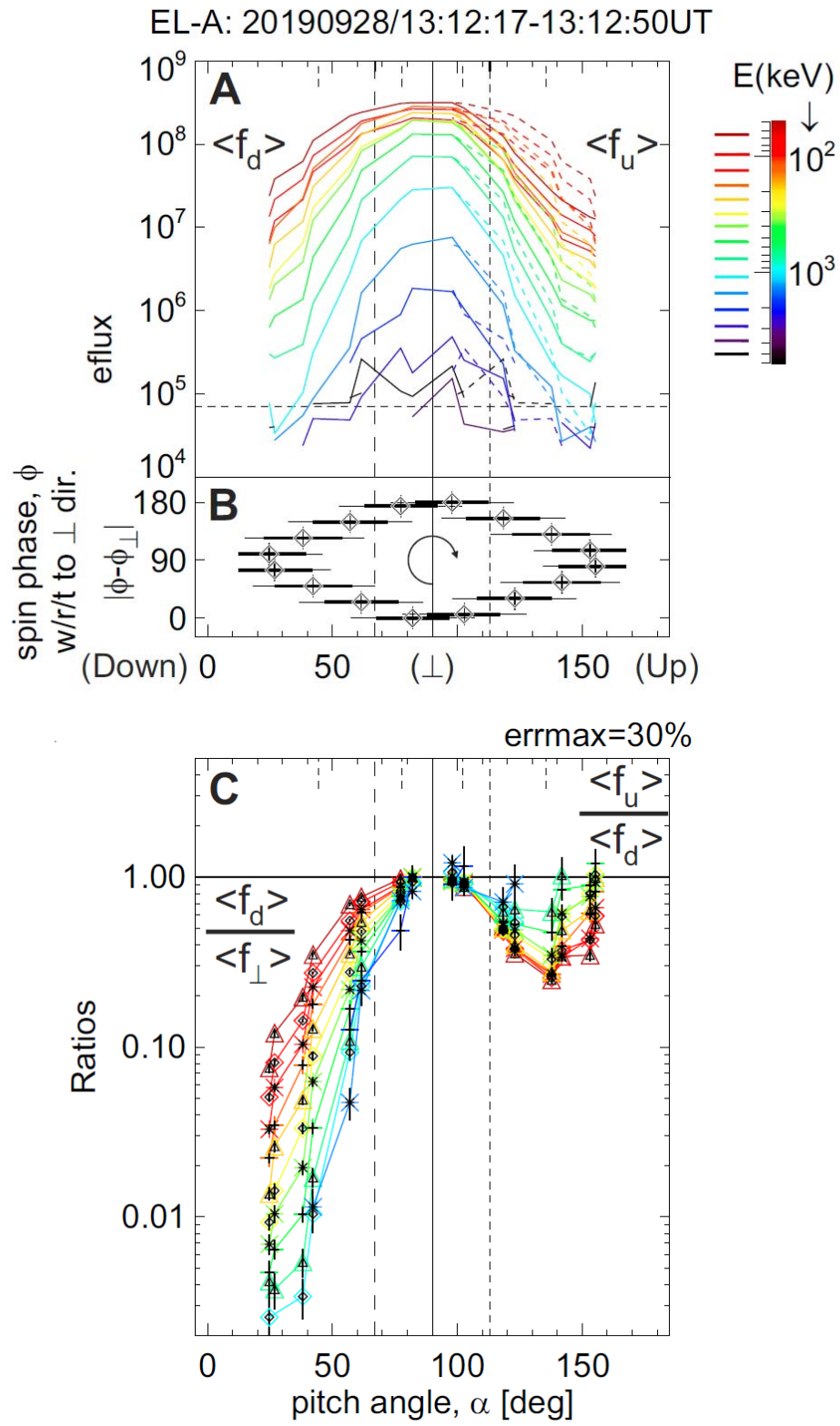
162

163

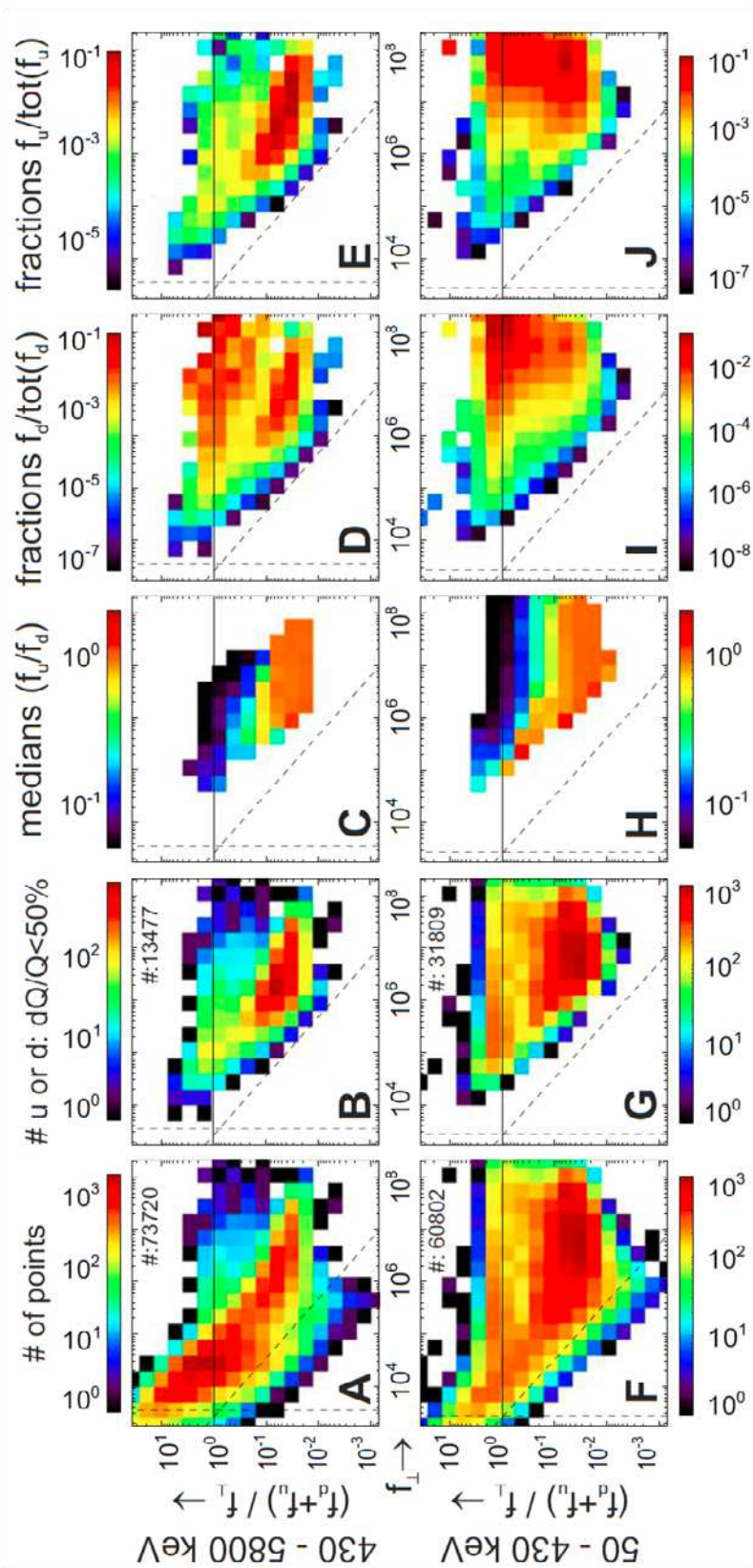
164



Extended Data Figure 2 | ELFIN-A dayside crossing of the outer radiation belt and auroral zone during the late recovery phase of a small storm. Format of Panels A-L is identical to that of Panels b-m in Figure 1. **(A-B)** Pitch-angle spectrograms of differential directional (broad) electron energy flux channels HiE and LoE (430-5800keV and 50-430keV, respectively). Upper solid and bottom dashed horizontal lines: loss cone ($\alpha=\alpha_{LC}$) and anti-loss cone ($\alpha=180^\circ-\alpha_{LC}$); middle solid line: $\alpha=90^\circ$. **(C-E)** Energy-time spectrograms of upgoing, trapped, and downgoing electron energy flux, respectively. **(F-H)** Energy-time spectrograms of upgoing-to-perpendicular (up-to-perp, f_u/f_\perp), downgoing-to-perpendicular (down-to-perp, f_d/f_\perp), and upgoing-to-downgoing (f_u/f_d) electron energy flux, respectively. **(I-J)** Energy flux in channels HiE and LoE, respectively (black: f_\perp ; blue: f_d ; red: f_u). **(K-L)** Ratios of energy flux in channels HiE and LoE, respectively (black: f_u/f_d ; blue: f_d/f_\perp ; red: f_u/f_\perp). Annotations denote L-shell (L), dipole magnetic local time (MLT), dipole magnetic latitude (MLA), and Universal Time (UT).



Extended Data Figure 3 | Veracity of loss-cone fluxes and their ratios. (A) Pitch-angle spectra of average fluxes from 11 spins (time interval indicated atop) for EPDE's logarithmically-equidistant energy channels from low (warmer colors) to high (colder colors) for ELFIN-A. Vertical lines denote pitch angles $\alpha=90^\circ$ (middle, solid), the loss cone ($\alpha=\alpha_{LC}$, left, long-dashed), and the anti-loss cone ($\alpha=180^\circ-\alpha_{LC}$, right, short-dashed). Dotted colored lines denote downgoing fluxes mirrored about pitch-angle $\alpha=0^\circ$ (i.e., plotted versus the supplementary of their pitch angles) for easy comparison with upgoing fluxes at the same energy (solid colored lines). The limits used to select field-aligned and perpendicular pitch-angle sector centers are four short dashed lines hanging down from the top of the panel. Two are 22.5° closer to the field-line direction than the loss and the anti-loss cone, respectively; two are 11.25° closer to perpendicular than the loss and the anti-loss cone, respectively. **(B)** Sector pitch angle, α (center, diamond), and width (acceptance angle, horizontal bar) as function of the sector center's spin-phase absolute distance from the (ascending) direction perpendicular to the magnetic field, $|\phi-\phi_\perp|$. The arrow in the centered circle denotes the direction of the detector's rotation in time during the spin. The thin horizontal bar centered at the diamond denotes the sector's pitch-angle full-width full max; the thick bar denotes its full-width half max. **(C)** Pitch-angle spectra of ratios of average fluxes for each energy channel (color) as determined from Panel A. The down-to-perpendicular ratio is on the left ($0^\circ<\alpha<90^\circ$); the upgoing-to-downgoing ratio is on the right ($90^\circ<\alpha<180^\circ$). Vertical dashed lines are same as in Panel A. Vertical bars at each point demarcate $\pm dr$, the absolute error value for each ratio r . Only points with $dr/r<30\%$ are shown.



207 **Extended Data Figure 4 (Rotate clockwise by 90°) | Statistical distribution of points, flux, and**
 208 **flux ratios.** All panels show distributions in two-dimensional (2D) space (f_{\perp} , $(f_d+f_u)/f_{\perp}$), where f_{\perp}
 209 is the differential directional energy flux (in $\text{keV}/\text{cm}^2 \text{ s str MeV}$) measured near $\alpha=90^\circ$ (trapped
 210 flux, perpendicular, \perp , to the **B** field) and (f_d+f_u) is the upward-plus-downward flux (in the loss
 211 cone and anti-loss cone). Top and bottom rows are for the HiE and LoE channels (430-5800keV
 212 and 50-430keV), respectively. Vertical dashed lines are the electronic noise flux values, f_{n_HiE}
 213 and f_{n_LoE} , for the HiE and LoE channels, respectively; diagonal dashed lines are the electronic
 214 noise divided by f_{\perp} . Measurements to the left of these lines are consistent with electronic noise.
 215 **(A, F)** Distribution of data in the database used (number of samples, #, indicated as an insert).
 216 **(B, G)** Distribution of data with statistically significant upgoing or downgoing fluxes ($df/f < 50\%$),
 217 which additionally eliminates samples corresponding to electronic noise. Note that most low f_{\perp}
 218 points have been eliminated from flux ratios in these and remaining 2D panels in the figure;
 219 averages computed from these statistically significant samples are intended to be
 220 representations of the total measured flux for the purpose of computing flux ratios, not the
 221 absolute flux. (Absolute flux depends on absolute detector efficiency, which has not yet been
 222 fully evaluated, but is not critical for this study). Panels (B, G) are the 2D versions of the PDFs
 223 for HiE and LoE in Figure 3a. **(C, H)** Distribution of medians of ratios f_d/f_u for statistically
 224 significant fluxes. As $(f_d+f_u)/f_{\perp}$ decreases, most medians increase from a few % to $\sim 100\%$ for
 225 most f_{\perp} values, particularly in cells with large numbers of points in Panels B and G. Panels (C, H)
 226 are the 2D versions of the median f_u/f_d lines in Figure 3a. **(D, I)** Distribution of the relative
 227 contribution to the total downgoing flux, f_d , by each cell in this 2D space. Two clusters of points
 228 with very weak dependence on f_{\perp} are evident: one near $(f_d+f_u)/f_{\perp} \sim 0.04$, which we attributed to

atmospheric scattering of trapped particles, and another near $(f_d+f_u)/f_{\perp}\sim 1$, which we attributed to magnetospheric scattering. These are the 2D versions of the line plots for HiE and LoE in Figure 3c. (E, J) Same as in Panels (D, I) except for the upgoing flux, f_u . The same two main populations are evident here, as well. These are the 2D versions of the line plots for HiE and LoE in Figure 3b.

237 **Extended Data Table 1**

Average Directional Electron Fluxes [†] and their Ratios							
All data in 3<L<7							
MLT	Energy [keV]	$r = \langle f_u \rangle / \langle f_d \rangle$	$\langle f_d \rangle / \langle f_{\perp} \rangle$	$\langle f_{\perp} \rangle$ [Units]	keV/cm ² s str MeV (Differential Directional Energy Flux)	Inferred [‡] Ratios	
Night	LoE: 50-430	9.3%	35.1%	1.65E+07		x=2f _a /f _m	2f _a /(2f _a +f _m) R=
	HiE: 430-5800	27.8%	8.3%	1.50E+06			
Day	LoE: 50-430	21.4%	16.3%	6.13E+06			
	HiE: 430-5800	81.2%	4.9%	5.55E+05			
Night+Day, Residence-time Norm'ed	LoE: 50-430	11.1%	30.0%	1.13E+07			
	HiE: 430-5800	37.5%	7.4%	1.03E+06		120%	55%
	50-5800 (Integral)	17.4%	17.3%	9.83E+06	keV/cm ² s str	42%	30%
D _{ST} < -20nT in 3<L<7							
MLT	Energy [keV]	$r = \langle f_u \rangle / \langle f_d \rangle$	$\langle f_d \rangle / \langle f_{\perp} \rangle$	$\langle f_{\perp} \rangle$ [Units]	keV/cm ² s str MeV (Differential Directional Energy Flux)	Inferred [‡] Ratios	
Night	LoE: 50-430	8.5%	35.7%	3.27E+07		x=2f _a /f _m	2f _a /(2f _a +f _m) R=
	HiE: 430-5800	22.7%	7.8%	2.37E+06			
Day	LoE: 50-430	23.2%	12.5%	1.16E+07			
	HiE: 430-5800	90.4%	3.9%	5.96E+05			
Night+Day, Residence-time Norm'ed	LoE: 50-430	10.2%	29.6%	2.21E+07			
	HiE: 430-5800	30.3%	7.0%	1.48E+06		87%	46%
	50-5800 (Integral)	13.8%	18.6%	1.64E+07	keV/cm ² s str	32%	24%

[†]Noise subtracted: f_{n,HiE}=3.48 10³, f_{n,LoE}=2.74 10³ [keV/cm² s str MeV]

[‡]where R=x/(x+1); r=x/(x+2)

Extended Data Table 1 | Differential and integral directional energy fluxes and ratios for the outer radiation belt (3<L<7) under all geomagnetic conditions (top) and for active (D_{ST}<-20nT) times (bottom). Ratios of time averages rather than medians of ratios have been used to accurately characterize total energy flux ratios. The combination of Night and Day ratios was determined directly from the numbers above them, assuming equal satellite residence time in the dayside and the nightside. The bottom row, which represents the integral directional energy flux channel (50-5800keV), was computed directly from the rows above it. f_u and f_d are upgoing and downgoing fluxes, <> represent averages, and f_a and f_m are the measured contributions to precipitation from atmospheric scattering and magnetospheric scattering. The

248 ratios x and R are the inferred net contributions to precipitation from atmospheric scattering
249 relative to magnetospheric scattering and relative to the total precipitation, respectively.

Figures

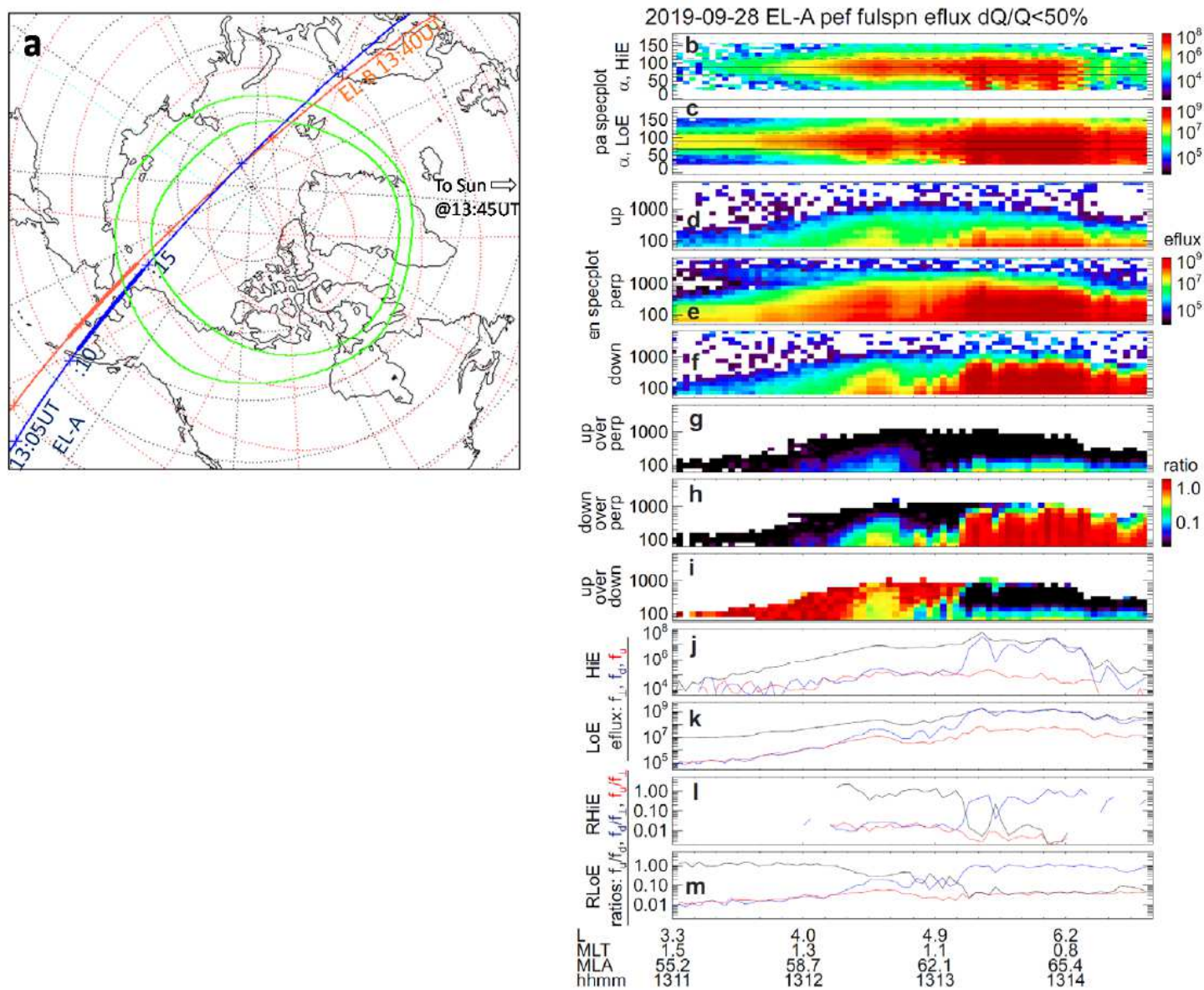


Figure 1

ELFIN storm time, nightside crossing of the outer radiation belt and auroral zone. Please see manuscript .pdf for full caption. Note: The designations employed and the presentation of the material on this map do not imply the expression of any opinion whatsoever on the part of Research Square concerning the legal status of any country, territory, city or area or of its authorities, or concerning the delimitation of its frontiers or boundaries. This map has been provided by the authors.

Directional differential energy flux ratios

Red: u/L ; blue: d/L ; black: u/d . Dashed: - - - Low AE; Solid: — High AE

MLT: noon \pm 4hrs

MLT: midnight \pm 4hrs

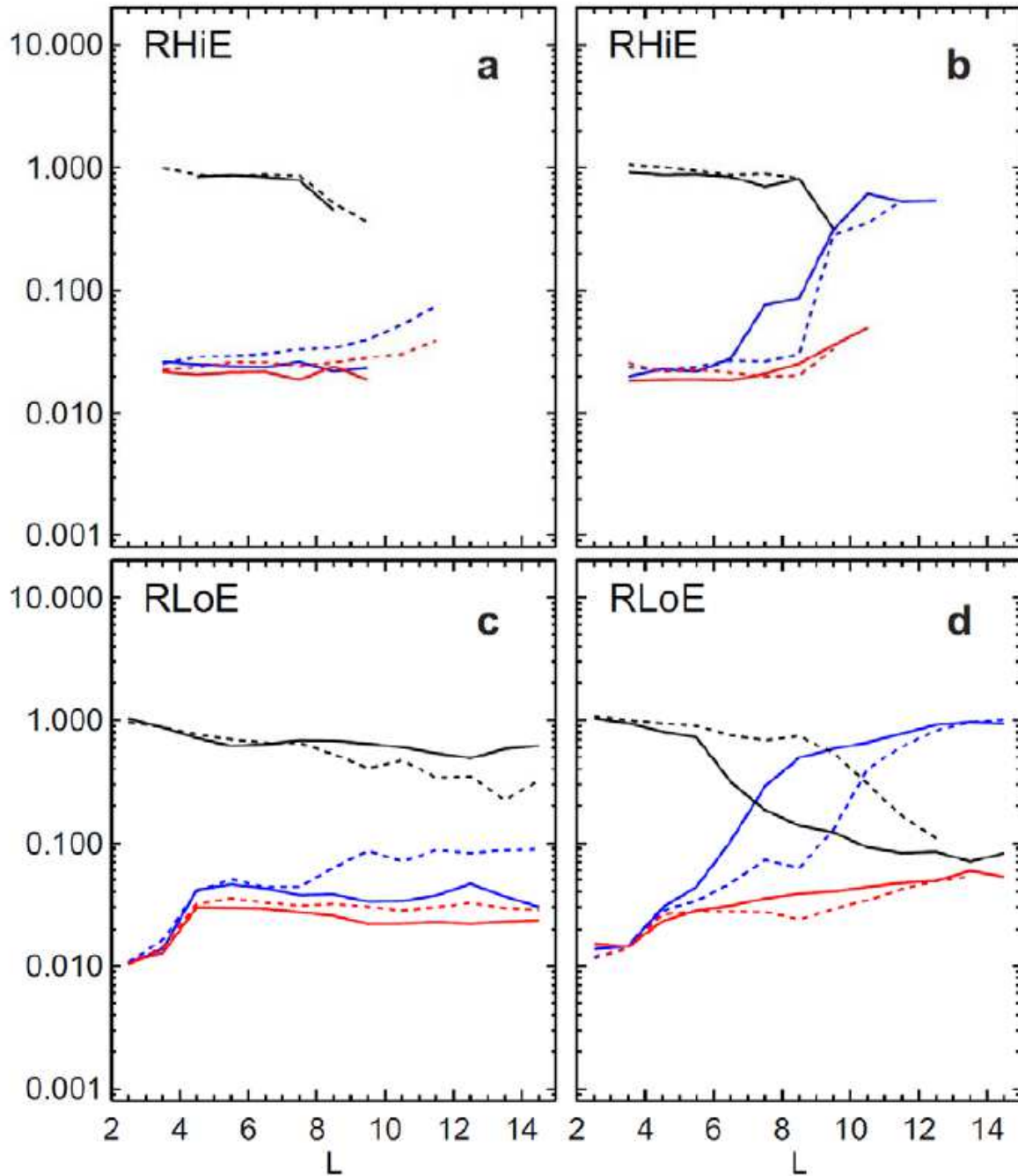


Figure 2

Dependence of energy flux ratios on L-shell, local time, and activity. Please see manuscript .pdf for full caption.

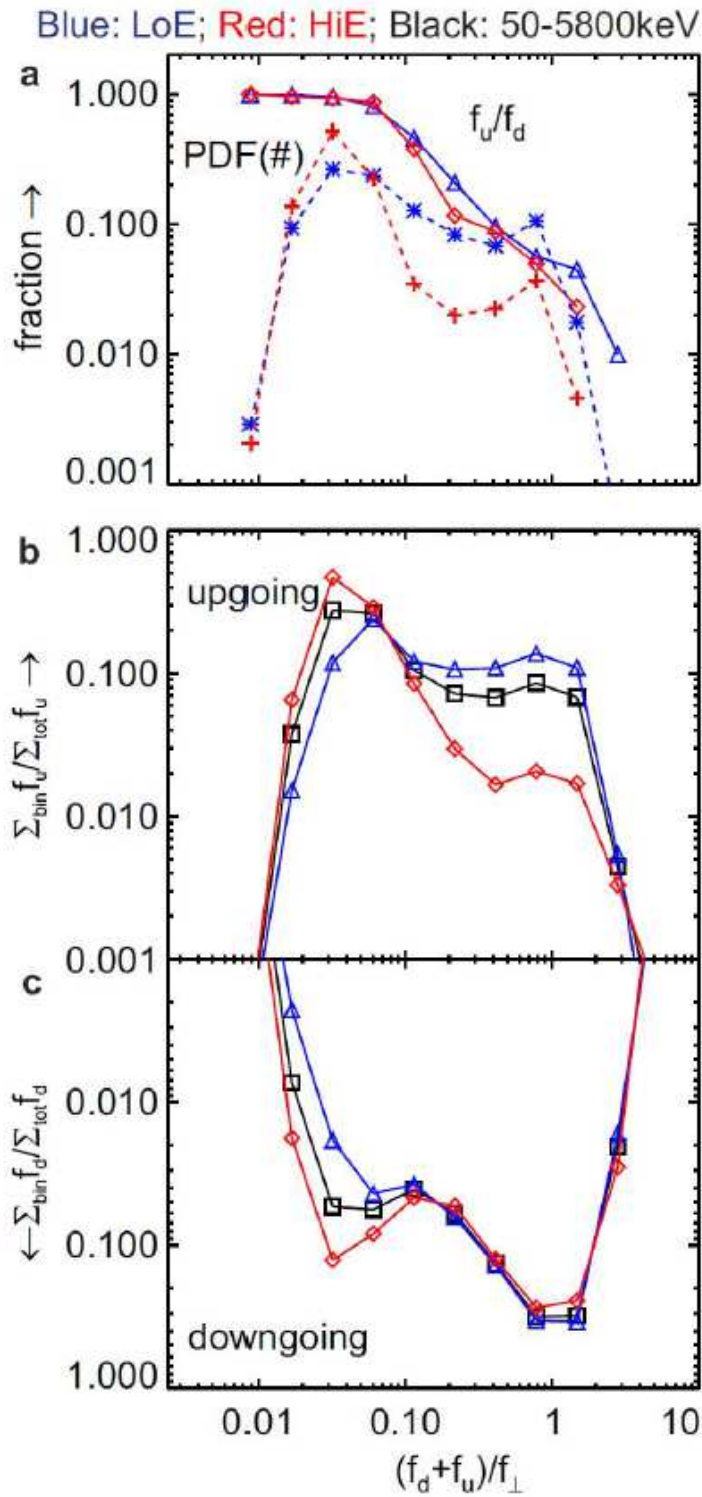


Figure 3

Distribution of data, fluxes, and flux ratios as a function of loss-cone flux. (a) Probability density functions of all data in the I50 and I430 channels (blue stars and red crosses, respectively) and medians of flux ratios (f_u/f_d) for these channels (blue triangles and red diamonds, respectively). (b) Relative contribution to net upward flux within the I50 and I430 broad differential broad energy channels (blue triangles and red diamonds, respectively) and within the summed energy channel representing the total

energy flux measured by the detector, i.e., at energies 50 keV – 5.8 MeV (black squares). (c) Same as in (c) but for the downward flux. Two-dimensional versions of several of these distributions, also plotted against the perpendicular energy flux, are shown in Extended Data Figure 4.